

Research Article

Daniel Holder*, Artur Leis, Matthias Buser, Rudolf Weber and Thomas Graf

High-quality net shape geometries from additively manufactured parts using closed-loop controlled ablation with ultrashort laser pulses

<https://doi.org/10.1515/aot-2019-0065>

Received November 30, 2019; accepted February 12, 2020; previously published online March 11, 2020

Abstract: Additively manufactured parts typically deviate to some extent from the targeted net shape and exhibit high surface roughness due to the size of the powder grains that determines the minimum thickness of the individual slices and due to partially molten powder grains adhering on the surface. Optical coherence tomography (OCT)-based measurements and closed-loop controlled ablation with ultrashort laser pulses were utilized for the precise positioning of the LPBF-generated aluminum parts and for post-processing by selective laser ablation of the excessive material. As a result, high-quality net shape geometries were achieved with surface roughness, and deviation from the targeted net shape geometry reduced by 67% and 63%, respectively.

Keywords: additive manufacturing; closed-loop control; laser powder bed fusion; optical coherence tomography; ultrashort pulsed laser ablation.

1 Introduction

Additive manufacturing comprises a wide range of different manufacturing processes. With laser powder bed fusion (LPBF) complex, metallic parts are generated from slices of selectively molten powder. The process offers a high flexibility with respect to the generation of highly individualized parts, bionic shapes, and light-weight construction [1, 2]. The produced parts,

however, typically deviate from the targeted net shape, to some extent, and exhibit high surface roughness values R_a in the order of 10–20 μm due to partially molten powder [3], build orientation, non-ideal process parameters, material shrinkage, and the staircase effect [4]. In particular, the staircase effect limits the precision of the manufactured parts, while the size of the powder grains determines the minimum thickness of the individual slices [5].

In order to improve precision and surface quality, different post-processing techniques and approaches were investigated [3, 5]. Laser-based approaches, such as laser polishing or laser ablation, have the advantage of avoiding significant mechanical impact on the post-processed parts. Laser polishing utilizes laser beam melting of the part's surface in order to smoothen the surface roughness by material flow. With this technique, the roughness of LPBF parts manufactured from AlSi10Mg powder could be reduced by about 92% to $R_a = 0.66 \mu\text{m}$ by scanning the surface with a cw laser, but the shape of the surface topography remained wavy [6]. Waviness and roughness can be further reduced with adapted scanning strategies, e.g. multiple scans with different scanning angles. However, repetitive remelting of the surface layer by laser polishing causes the formation of a growing heat-affected zone [7]. This effect can be avoided using laser ablation with short or ultrashort laser pulses, thanks to the reduced thermal load outside the ablation zone. Laser ablation with an ns laser allowed to reduce the roughness R_a of LPBF-generated steel parts from 19 μm to 5 μm and demonstrated that the roughness decreases with an increasing number of passes [8]. An approach using an fs laser and a CCD-based imaging system to control the beam position during the ablation of LPBF-generated parts is presented in Ref. [9]. Ablation of multiple layers with adapted focal position allowed to remove most of the powder grains on the surface and reduced the roughness R_a from 22 μm to below 3 μm . Furthermore, the circularity of holes that were manufactured in the LPBF process was improved by the removal of excessive material.

*Corresponding author: Daniel Holder, University of Stuttgart, Institut für Strahlwerkzeuge (IFSW), Stuttgart, Baden Württemberg, Germany, e-mail: daniel.holder@ifsw.uni-stuttgart.de

Artur Leis, Matthias Buser, Rudolf Weber and Thomas Graf: University of Stuttgart, Institut für Strahlwerkzeuge (IFSW), Stuttgart, Baden Württemberg, Germany

www.degruyter.com/aot

© 2020 THOSS Media and De Gruyter

 Open Access. © 2020 Daniel Holder et al., published by De Gruyter.  This work is licensed under the Creative Commons Attribution 4.0 Public License.

Laser ablation cannot only be used to reduce surface roughness but also to change the macroscopic geometry of the parts by an automated process using optical coherence tomography (OCT) in combination with a galvanometer scanner in order to measure the actual geometry of the post-processed part and determine where further ablation is required [10]. The integration of the OCT-based measurements into a closed-loop control allowed the automated machining of a fabric texture on the original flat steel surface and the reduction of surface roughness compared to open-loop control. Webster et al. utilized a similar setup but with fixed optics for automated laser micromachining of heterogeneous materials, e.g. bone and wood. As a result, a remaining root-mean-square (RMS) deviation of the machined depth compared to the designed depth of $14\ \mu\text{m}/\text{pixel}$ for bone and $35\ \mu\text{m}/\text{pixel}$ for wood could be achieved for a spiral-shaped geometry [11]. The suitability of OCT-based closed-loop controlled ablation of heterogeneous material was also demonstrated by Boley et al. for precise machining of carbon fiber-reinforced plastics (CFRP) with unidirectional fibers. Compared to the open-loop controlled process, the surface roughness S_a could be reduced from $60\ \mu\text{m}$ to $7\ \mu\text{m}$, and the maximum deviation from the targeted depth was reduced from $200\ \mu\text{m}$ to $20\ \mu\text{m}$ [12]. In addition, the OCT-based measurement enables the determination of the fiber's orientation for layer-accurate laser ablation of CFRP with multidirectional fibers [13] and the detection of the position of the processed part in the working area of a processing station, e.g. during a laser beam decoating process [14].

The described applications show the high potential of OCT-based measurements and closed-loop control during laser ablation of various materials. In the following, we present OCT-based closed-loop controlled laser ablation of LPBF-generated aluminum parts with ultrashort laser pulses in order to reduce the surface roughness and improve the geometrical accuracy. The OCT-based measurements were used for both the precise positioning of the workpiece and to determine the areas where further ablation is required to reach the targeted net shape of the additively produced parts. This approach combines the advantages of additive and subtractive laser manufacturing processes in order to create 3D-shaped geometries with high freedom of design and high precision. Section 2 presents the components and methods that are required for closed-loop controlled laser ablation of additively manufactured aluminum parts with ultrashort laser pulses and the analysis of the post-processed parts regarding their surface roughness and shape deviation. The impact of different peak fluences on the resulting surface roughness and microstructure of flat LPBF-generated aluminum parts is discussed in Section 3

in order to determine suitable process parameters for the shape enhancement of various 3D-shaped geometries. Finally, the presented approach is evaluated with regard to the removal of surface defects and the achievable accuracy of manufacturing different geometries.

2 Methods

The approach of creating precise 3D-shaped geometries by first additive and then subtractive laser manufacturing processes is shown schematically in Figure 1. Two different processing stations had to be utilized in order to manufacture the parts by LPBF (Figure 1A) and post-process the parts by closed-loop controlled laser ablation with ultrashort laser pulses (Figure 1D). Therefore, selective and local post-processing by controlled ablation requires precise positioning of the previously manufactured raw part with respect to the laser processing beam. With OCT-based measurements, positioning can be achieved with an accuracy of a few microns. This was achieved with an iterative procedure in which the processing field was measured, the current position of the workpiece compared with the target position (black dotted line in Figure 1B), and the part moved and rotated until the deviations of current position and target position were minimized. The center of the processing field was defined as target position for processing of the part, as large deflection angles of the OCT beam caused errors in the OCT-based measurements. The target geometry for the controlled ablation process was identical to the one of the LPBF process, but with an axial offset of $z=400\ \mu\text{m}$ shifted into the part (Figure 1C) in order to assure that the whole part is ablated at least for a few scans, as this removed most of the powder grains in Ref. [9].

2.1 Additive manufacturing of aluminum parts

The parts were manufactured from an AlSi10Mg powder with a grain size between $20\ \mu\text{m}$ and $56\ \mu\text{m}$. The LPBF process was performed in a TruPrint 3000 machine from Trumpf (Ditzingen, Germany) in the transient regime between heat conduction and deep penetration welding at an average laser power of $430\ \text{W}$ focused onto the powder bed with a beam diameter of $100 \pm 5\ \mu\text{m}$. The beam was moved over the powder bed with a feed rate of $1300\ \text{mm/s}$ and a hatching distance of $180\ \mu\text{m}$ generating layer thicknesses of about $60\ \mu\text{m}$. Nitrogen was used as inert gas to avoid oxidation. The temperature of the substrate plate was constantly kept at 200°C .

Two different geometries were manufactured. The first one, a simple plane part, was processed with various peak fluences in order to investigate their impact on the resulting surface topography. The roughness of the plane sample before post-processing was measured to be $S_a = 14.1 \pm 1.7\ \mu\text{m}$, which is consistent with typically achieved roughness values of additively manufactured parts [5]. The second one, a more complex geometry, is shown in Figure 2 and includes different challenges when creating additively manufactured 3D-shaped parts. Inclined surfaces with different orientations (e.g. cone, pyramid) and inclination angles (e.g. half sphere) are used to investigate the staircase effect. Sharp edges (e.g. pyramid), steep transitions (e.g. steps), and thin tip (e.g. cone, pyramid) are suitable to determine the

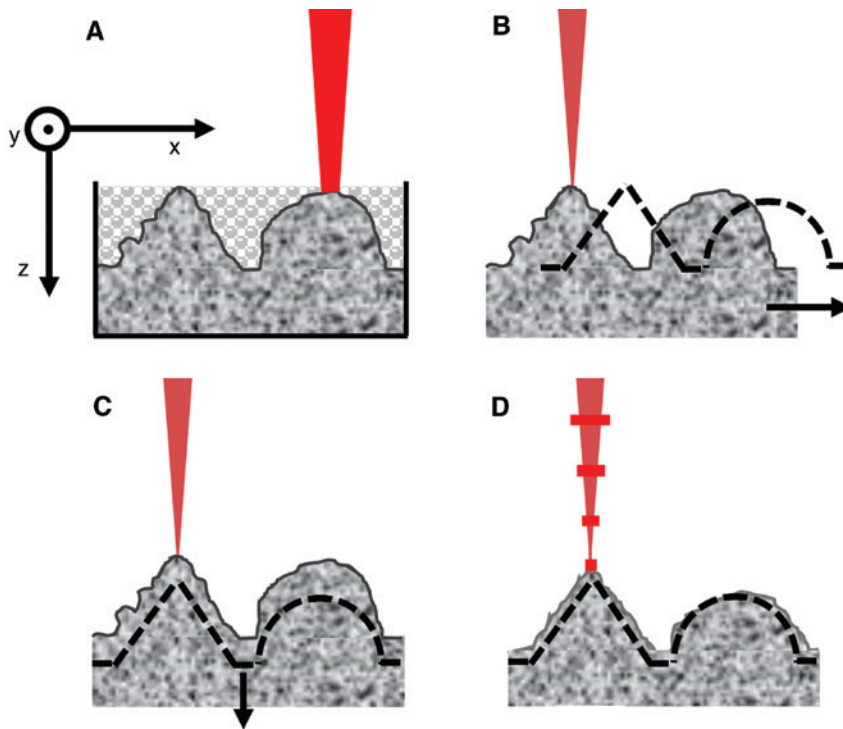


Figure 1: The different steps of the used manufacturing process of 3D-shaped parts: (A) LPBF process of the raw part with a cw laser; (B) positioning of the raw part with the help of OCT measurements to match to the position of the target geometry; (C) axial offset of target geometry; (D) Post-processing of the raw part with OCT-based closed-loop controlled ablation using ultrashort laser pulses.

achievable precision regarding the manufacturing of given geometrical features. The lateral dimensions of the sample geometry were $8 \times 8 \text{ mm}^2$ with a maximum height of 1.5 mm. The grayscale of the geometry shown in Figure 2 is linearly scaled between maximum height (white, 1.5 mm) and minimum height (black, 0 mm).

2.2 Closed-loop controlled ablation with ultrashort laser pulses

The setup for post-processing by means of closed-loop controlled laser ablation consists of three major components: the OCT system to

detect the location of the surface and the shape of the workpiece, the processing laser system, and the control system.

Optical measurements of the surface were performed with the Fourier-domain OCT-based system CHRcodile 2 from Precitec (Gaggenau, Germany), which provides an axial measurement range of about 6 mm. The measuring rate was set to 70 kHz.

The processing laser system Femto 30 from FiberCryst (Décines-Charpieu, France) used for post-processing of the additively manufactured aluminum parts in this study emits laser pulses at a wavelength of 1030 nm and linear polarization with a pulse duration of $\tau_p = 600 \text{ fs}$ and a beam quality factor $M^2 < 1.3$. The laser system was operated at the same repetition rate $f_p = 70 \text{ kHz}$ as the measuring rate of the OCT in order to be able to measure the changes in the surface induced by

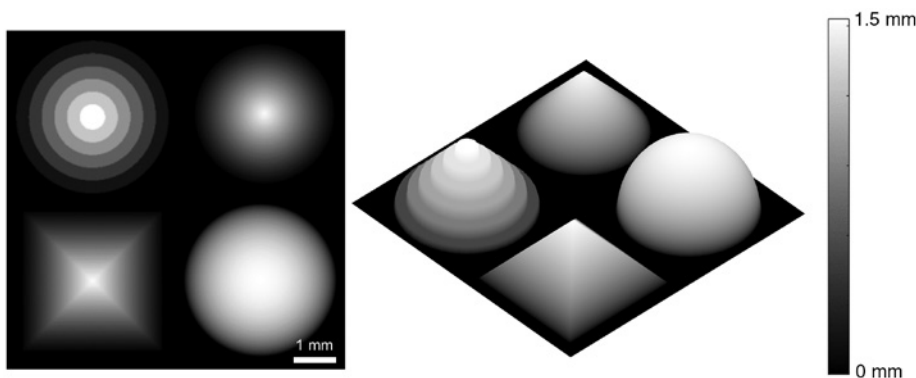


Figure 2: Grayscale image of the target geometry from plan view and oblique view.

every single applied laser pulse. Pulse energies of up to 85.7 μJ were used in the ablation experiments, corresponding to a maximum average power of 6 W.

The beams of the OCT and the processing laser were superposed by means of a dichroic mirror as shown schematically in Figure 3. The dichroic mirror was HR-coated for the beam of the processing laser at a wavelength of $\lambda_{\text{pl}}=1030$ nm and AR-coated for the beam of the OCT centered at a wavelength of $\lambda_{\text{OCT}}=1080$ nm. Both beams were guided through a galvanometer scanner system (IntelliSCAN 30, Scanlab, Puchheim, Germany) for deflection. The focal length of the used F-Theta lens (Sill Optics, Wendelstein, Germany) was 163 mm resulting in focal diameters of 50 ± 5 μm for the processing laser and 15 ± 5 μm for the beam of the OCT.

The pulse overlap in, and perpendicular to, the scanning direction was kept at 84% in order to avoid heat accumulation effects by pulse-to-pulse or scan-to-scan accumulation [15]. This was achieved using a feed rate of $v=560$ mm/s and a hatching distance of 8 μm . The principle of the control system was already introduced in Refs. [12] and [13].

2.3 Analysis of surface roughness and shape deviation

Six different orders of shape deviations are defined in DIN 4760. The shape deviations are differentiated according to spatial dimensions and range from deviations of the characteristic dimensions of the part, e.g. increased length or thickness in the first order to increased surface roughness in the fourth order and the crystal structure in the sixth order [16]. In this work, the surfaces of the additively manufactured parts with and without post-processing by OCT-controlled ablation were analyzed with regard to shape deviations of the first and the fourth order using a Keyence 3D-Laser Scanning Microscope (LSM) VK-9710-K. Furthermore, the microstructure of the surface was investigated using a scanning electron microscope (SEM) Joel JSM-6490LV.

Using an objective with a magnification of 20 on the LSM for the measurement of the roughness led to a lateral resolution of 0.69 μm /pixel. The axial scanning pitch was 0.2 μm . The arithmetical mean height

$$S_a = \frac{1}{MN} \sum_{m=1}^M \sum_{n=1}^N |z(x_m, y_n) - \langle z \rangle|, \quad (1)$$

where z is the height measured at the coordinates x and y , and M and N are the number of pixels, determined according to EN ISO 25178 and

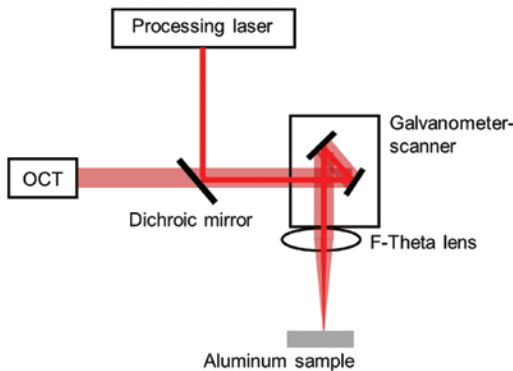


Figure 3: Setup of the OCT-based closed-loop controlled laser ablation processes.

was used to assess the effectiveness of the closed-loop controlled ablation with respect to the reduction of the surface roughness and, hence, the reduction of fourth-order deviations for additively manufactured parts. The effectiveness was investigated for different peak fluencies

$$\phi_0 = \frac{2E_p}{\pi w_0^2}, \quad (2)$$

where E_p is the pulse energy, and w_0 is the radius of the processing laser beam. For the evaluation of the first-order deviations from the net shape, an objective with a magnification of 10 was used, leading to a lateral resolution of 1.38 μm /pixel. The axial scanning pitch was 0.2 μm . The mean deviation was calculated by

$$D_a = \frac{1}{MN} \sum_{m=1}^M \sum_{n=1}^N |z(x_m, y_n) - z_t(x_m, y_n)|, \quad (3)$$

where z_t is the targeted height of the workpiece.

3 Quality enhancement of additively manufactured parts by closed-loop controlled laser ablation with ultrashort laser pulses

3.1 Smoothing of surface topography

Squared areas of 1×1 mm² were ablated on the plane samples using the setup and parameters described in Section 2.2 with different peak fluencies ranging from 0.2 J/cm² to 8.6 J/cm². The targeted ablation depth of the closed-loop controlled post-processing was set to 100 μm . The number of slices to achieve the targeted ablation depth varied between 70 and 300, depending on the applied peak fluence. The lowest peak fluence of 0.2 J/cm² required 300 slices, and the highest peak fluence of 8.6 J/cm² required 70 slices to reach the targeted depth of 100 μm . The impact of the peak fluence on the mean height S_a and the microstructure is shown in Figures 4 and 5, respectively. The areas for the measurements by LSM and SEM were manually selected to represent the overall surface of the processed area.

The application of $\Phi_0=0.2$ J/cm² leads to $S_a=14.5 \pm 3.4$ μm , which is close to the roughness value of $S_a=14.1 \pm 1.7$ μm of the non-ablated surface. However, the microstructures of these surfaces differ in shape and size, as shown in Figure 5A and B. Solidified melt drops, probably due to spatter formation during the LPBF process, and adhering powder grains are present on the non-ablated surface. The surface irradiated with 0.2 J/cm² contains no solidified melt drops and shows a coarse surface with partially removed material, leading to cavities with a depth of up to 30 μm .

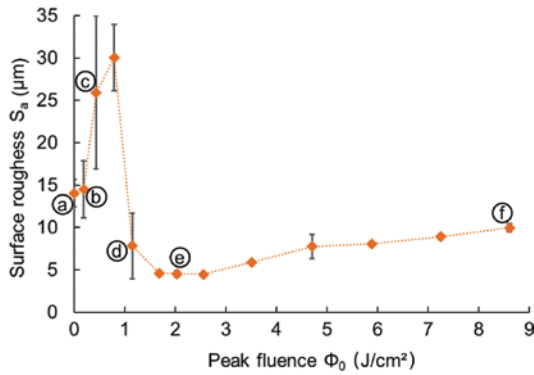


Figure 4: Measured roughness S_a as a function of the applied peak fluence. The dashed line was inserted to guide the eye. The value at 0 J/cm² represents the surface roughness of a non-ablated area on the test sample. Data points with corresponding SEM images in Figure 5 are marked with (A–F). Laser wavelength $\lambda_{pl} = 1030$ nm, pulse duration $\tau_p = 600$ fs, repetition rate $f_p = 70$ kHz, feed rate $v = 560$ mm/s.

The application of peak fluences exceeding $\Phi_0 = 0.4$ J/cm² and $\Phi_0 = 0.8$ J/cm² significantly increases the measured surface roughness to $S_a = 25.9 \pm 9.0$ μm and $S_a = 30.1 \pm 3.9$ μm, respectively. The inhomogeneous material removal results in cavities as deep as 100 μm and the increased roughness S_a (Figure 5C). The growth of the cavities is probably partially initiated by particles on top of the protrusions, which act as light scattering centers. Increasing the applied peak fluence to $\Phi_0 = 1.2$ J/cm² leads to a significant reduction in the roughness to $S_a = 7.8 \pm 3.9$ μm, much lower than the initial value of $S_a = 14.1 \pm 1.7$ μm. Homogeneous material removal yields a smoothed surface without large cavities and a reduced number of protrusions as can be seen in Figure 5D. However, individual protrusions remain, which, in combination with observations at lower peak fluence, leads to the assumption that the complete removal of the protrusions require higher peak fluences. Additionally, small holes with a

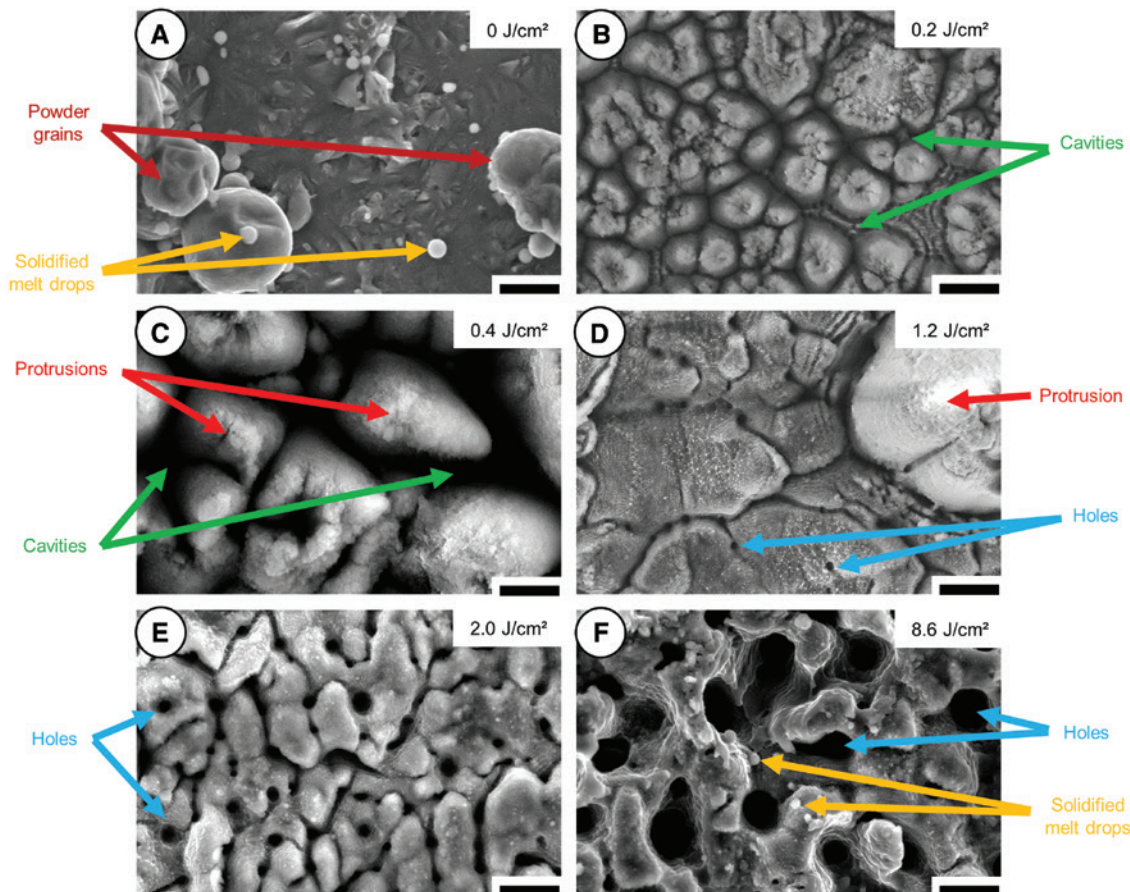


Figure 5: Microstructure of the LPBF-generated test sample measured by the SEM after post-processing with different applied peak fluences between 0.2 and 8.6 J/cm² (A–F). Scale bars represent a length of 20 μm. Laser wavelength $\lambda_{pl} = 1030$ nm, pulse duration $\tau_p = 600$ fs, repetition rate $f_p = 70$ kHz, feed rate $v = 560$ mm/s.

diameter of 3–5 μm and a depth of up to 10 μm can be seen in the grooves on the surface next to the remaining protrusion in Figure 5D.

The lowest surface roughness of $S_a = 4.6 \pm 0.3 \mu\text{m}$ was achieved within the range of $1.7 \text{ J/cm}^2 < \Phi_0 < 2.6 \text{ J/cm}^2$, where no protrusions or large cavities remained on the surface, as can be seen in Figure 5E. The diameter and depth of the holes on the surface are increased to 4–6 μm and 25 μm , respectively.

With peak fluences exceeding 2.6 J/cm^2 , the measured roughness is increased again due to the increased diameter and greater depth of the holes. This can be seen particularly well in Figure 5F in the form of a fissured surface with holes, with diameters of up to 20 μm , leading to a surface roughness of $S_a = 10.0 \pm 0.5 \mu\text{m}$. Furthermore, solidified melt drops can be seen again on the surface in between the holes, indicating an explosive melt ejection process, which was also observed in Ref. [17] at high irradiated peak fluences. The impact of peak fluences above 1.2 J/cm^2 on the modulation period of the microstructure is consistent with the observations for the irradiation of steel with femtosecond laser pulses shown in Ref. [18]. Peak fluences in the range between 1.7 J/cm^2 and 2.6 J/cm^2 should be applied in order to reduce the roughness S_a by 67% compared to the original surface.

3.2 Creating high-quality net shape geometries

The additively manufactured part of the 3D-shaped geometry shown in Figure 1 was positioned according to the method presented in Section 2. The beam was focused on the highest position of the raw part ($z = 0 \mu\text{m}$), where the peak fluence was set to $\Phi_0 = 3.5 \text{ J/cm}^2$, as the focus position could not be adjusted within the control algorithm. The effective peak fluence on the workpiece is reduced with increasing ablation depth due to the divergence of the beam, but the peak fluence did not fall below the range of $1.7 \text{ J/cm}^2 < \Phi_0 < 2.6 \text{ J/cm}^2$ needed to achieve the minimum roughness as shown in Figure 4. On average, about 400 μm were ablated using a peak fluence of $\Phi_0 = 3.5 \text{ J/cm}^2$ and 1140 slices.

The SEM image of the cone-shaped geometry after the LPBF process is seen in Figure 6A. Several powder grains are present on the surface of the raw part, and the tip is rounded off. The quantified deviations of the raw part from the targeted net shape are shown in Figure 6B. The green color corresponds to small deviations of less than $\pm 15 \mu\text{m}$ and represents a high conformity of

the manufactured part with the targeted geometry. Positive deviations of up to 150 μm (dark red) reveal excessive material on the surface of the measured part, e.g. adherent, partially molten powder grains, which are present in the border areas of the image. Correspondingly, negative deviations of up to $-150 \mu\text{m}$ (dark blue) reveal missing material of the measured part, e.g. a thin tip that is too small to be manufactured in the LPBF process due to slicing and minimum size of the powder grains. The slicing also prevents the manufacturing of smooth inclined surfaces, indicated by the ring-shaped deviations in Figure 6B. These artifacts are also the reason for the rather high mean deviation $D_a = 38.2 \mu\text{m}$ of the raw part compared to $D_a = 14.3 \mu\text{m}$ of the post-processed part. The SEM image of the post-processed part is shown in Figure 6C. It does not have any partially molten powder grains adhering to the surface and exhibits a pronounced tip and a smooth conical surface. This visual impression is confirmed by the quantified deviation chart in Figure 6D. Some remaining excessive material in the order of 20 μm –40 μm and a number of very small spots with deviations up to $\pm 100 \mu\text{m}$ can be seen near the tip. As these dots are not seen in the SEM picture (C), it can be assumed that these are measurement artifacts of the LSM.

Powder grains on the surface, a rounded off tip and wavy surface are also seen in the SEM and the deviation plot of the pyramid-shaped raw part in Figure 7A, B. The edges of the pyramid deviate by $-100 \pm 25 \mu\text{m}$ (dark blue). As was the case with the tip, the cause of the deviations on the edges of the pyramid are again found in the LPBF process due to slicing and the minimum size of the powder grains. The additional deviations on the edges lead to a significantly higher mean deviation of $D_a = 43.5 \mu\text{m}$ compared to the cone-shaped geometry with $D_a = 38.2 \mu\text{m}$. In contrast to this, the mean deviation of the pyramid-shaped post-processed part with $D_a = 14.9 \mu\text{m}$ is close to $D_a = 14.3 \mu\text{m}$ of the cone-shaped geometry, indicating that edges on inclined surfaces in the target geometry can well be manufactured by post-processing. This is also revealed by the SEM image and the deviation plot in Figure 7C and D that show no significant deviations in the area of the edges.

The SEM and deviation images of the step-shaped geometry are shown in Figure 8. High positive and negative deviations with irregular-shaped steps of the raw LPBF-generated part can be seen in the SEM image in Figure 8A. The radii of the different circular steps are about 50 μm smaller than specified with the target geometry, which was caused due to the limited minimum feature size in the LPBF process. Deviations

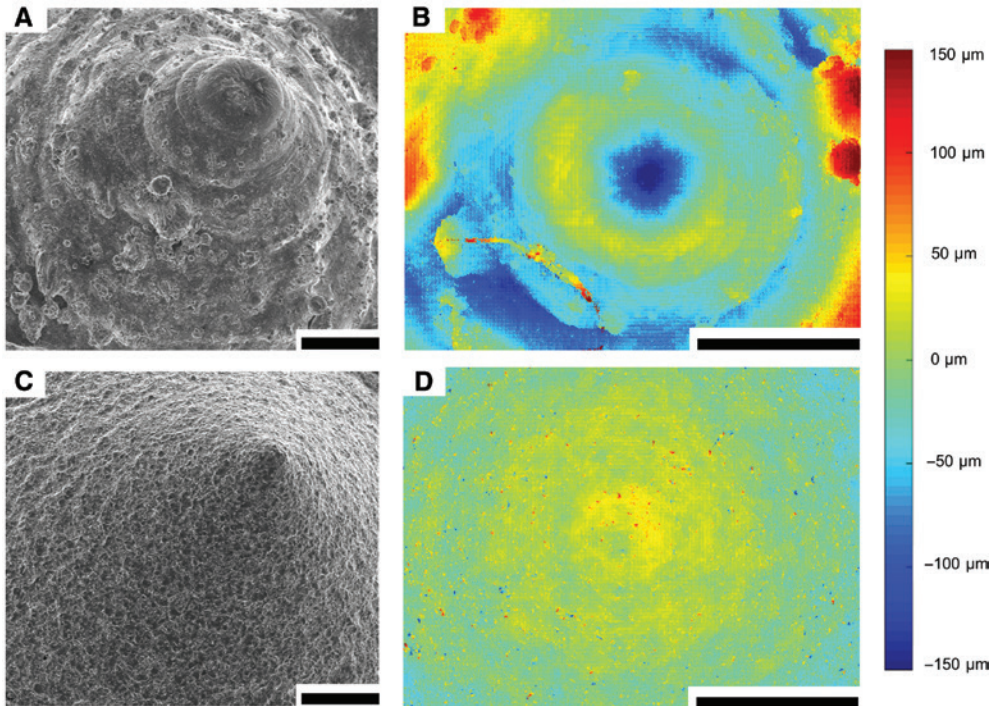


Figure 6: Cone-shaped geometry: (A) SEM image (oblique view) of the raw part manufactured by LPBF. (B) Deviation of the raw part from the targeted geometry measured by LSM. (C) SEM image (oblique view) of the post-processed part. (D) Deviation of the post-processed part from the targeted net shape measured by LSM. Scale bars represent a length of 500 μm . Laser wavelength $\lambda_{PL} = 1030$ nm, pulse duration $\tau_p = 600$ fs, peak fluence $\Phi_0 = 3.5$ J/cm², repetition rate $f_p = 70$ kHz, feed rate $v = 560$ mm/s.

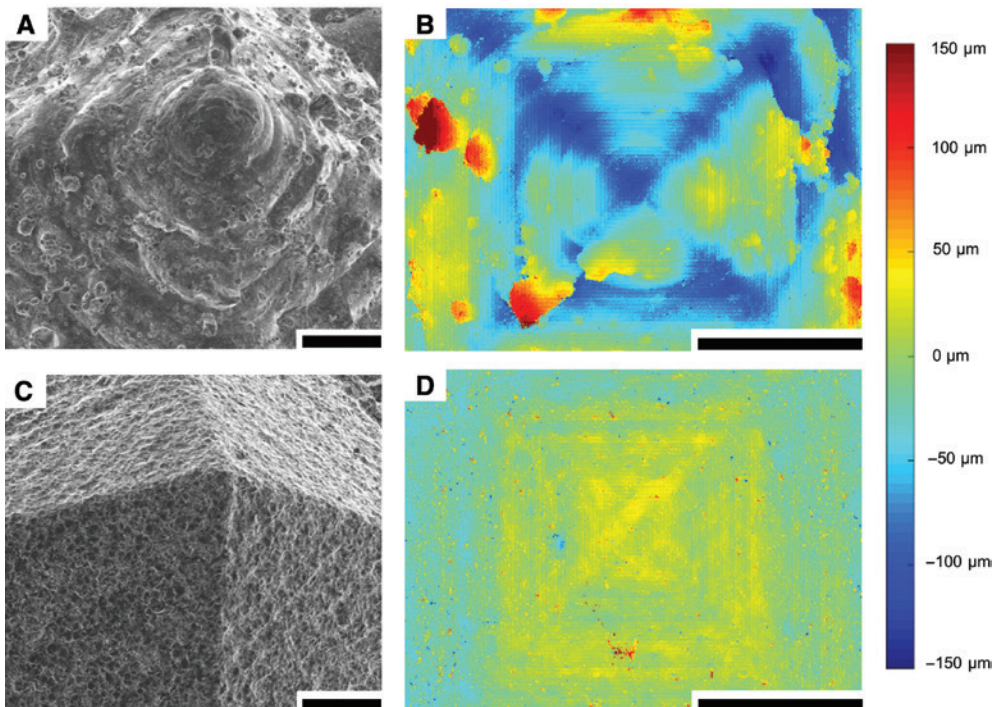


Figure 7: Pyramid-shaped geometry: (A) SEM image (oblique view) of the raw LPBF-generated part. (B) Deviation of the raw part from the target geometry measured by LSM. (C) SEM image (oblique view) of post-processed part; (D) Deviation of the post-processed part from target geometry measured by LSM. Scale bars represent a length of 500 μm . Laser wavelength $\lambda_{PL} = 1030$ nm, pulse duration $\tau_p = 600$ fs, peak fluence $\Phi_0 = 3.5$ J/cm², repetition rate $f_p = 70$ kHz, feed rate $v = 560$ mm/s.

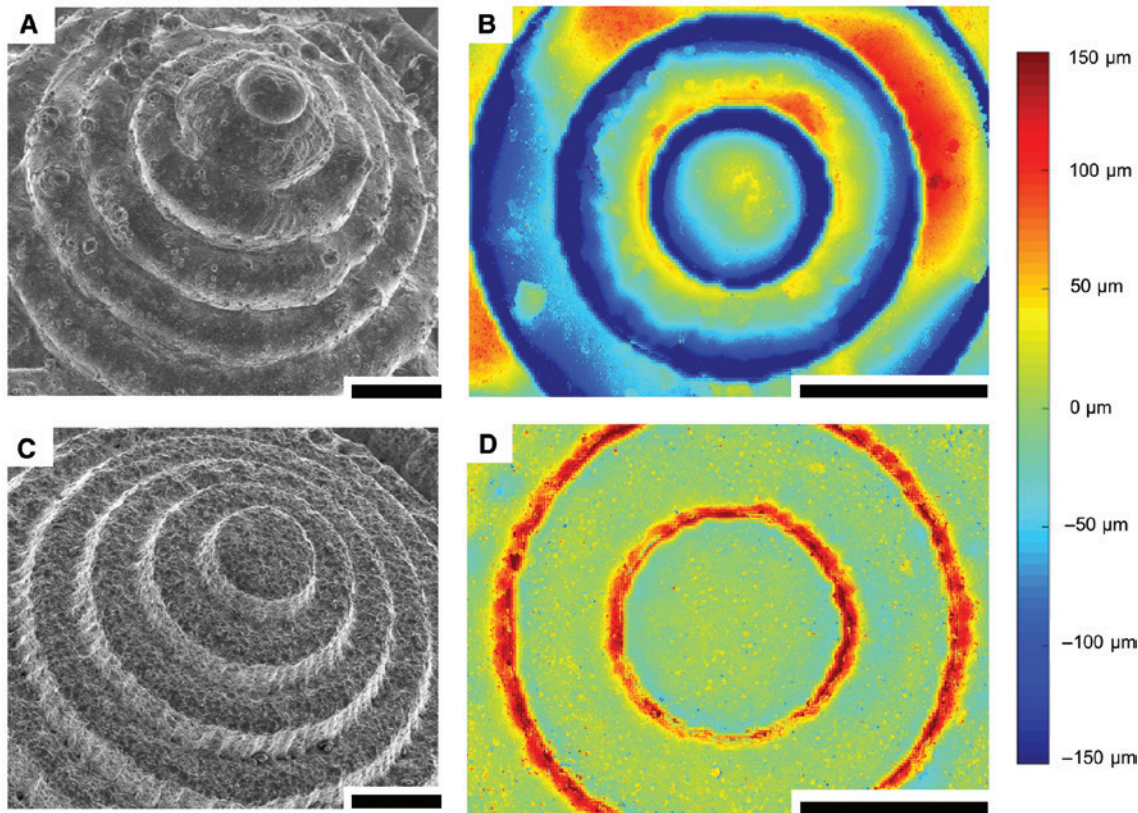


Figure 8: Step-shaped geometry: (A) SEM image (oblique view) of raw LPBF-generated part. (B) Deviation of the raw part from the target geometry measured by LSM. (C) SEM image (oblique view) of the post-processed part. (D) Deviation of the post-processed part from target geometry measured by LSM. Scale bars represent a length of 500 μm . Laser wavelength $\lambda_{\text{pl}} = 1030 \text{ nm}$, pulse duration $\tau_{\text{p}} = 600 \text{ fs}$, peak fluence $\Phi_0 = 3.5 \text{ J/cm}^2$, repetition rate $f_{\text{p}} = 70 \text{ kHz}$, feed rate $v = 560 \text{ mm/s}$.

of $\pm 30 \mu\text{m}$ from the targeted step height of $250 \mu\text{m}$ resulted from the layer thickness of $60 \mu\text{m}$, as the layer thickness is not an integer divider of the step height. The edges of the steps are rounded off due to the surface tension of the liquid melt in the LPBF process, preventing the manufacturing of sharp edges and steep flanks. These limits of the LPBF process cause a high mean deviation of $D_a = 74.7 \mu\text{m}$, which can be reduced to $D_a = 23.5 \mu\text{m}$ by post-processing. Although the radii of the raw part were about $50 \mu\text{m}$ too small, the radii and height of the different steps of the post-processed part are consistent with those of the target geometry. This was enabled by the axial offset of the target geometry of $400 \mu\text{m}$ into the workpiece, resulting in enough material available for compensation. However, a taper angle is present on the sidewalls between two adjacent steps, which is represented as an excessive material (dark red) in Figure 8D. The formation of a taper angle is a well-known phenomenon from laser drilling and cutting [19], which can be minimized using helical optics [20].

The SEM and deviation image of the half-sphere-shaped geometry are shown in Figure 9. The deviations of the raw part from the target geometry are mainly caused by excessive material on the surface, again due to adherent powder grains and the minimum layer thickness of the LPBF process. The mean deviation was calculated to be $D_a = 43.2 \mu\text{m}$. These deviations were effectively removed by post-processing, resulting in a smooth surface and a low mean deviation of $D_a = 9.9 \mu\text{m}$.

The investigations confirm the high potential of OCT-based closed-loop controlled laser ablation with ultrashort laser pulses for manufacturing of different high-quality net shape geometries from LPBF-generated aluminum parts. Depending on the geometry, the mean deviation was reduced by at least 63% by selective ablation of excessive material resulting from the slicing in the LPBF process. Features like thin tips, smooth inclined surfaces, and pronounced edges can be realized using the presented approach. The results show the great potential that is offered by combining different laser-based manufacturing processes [21].

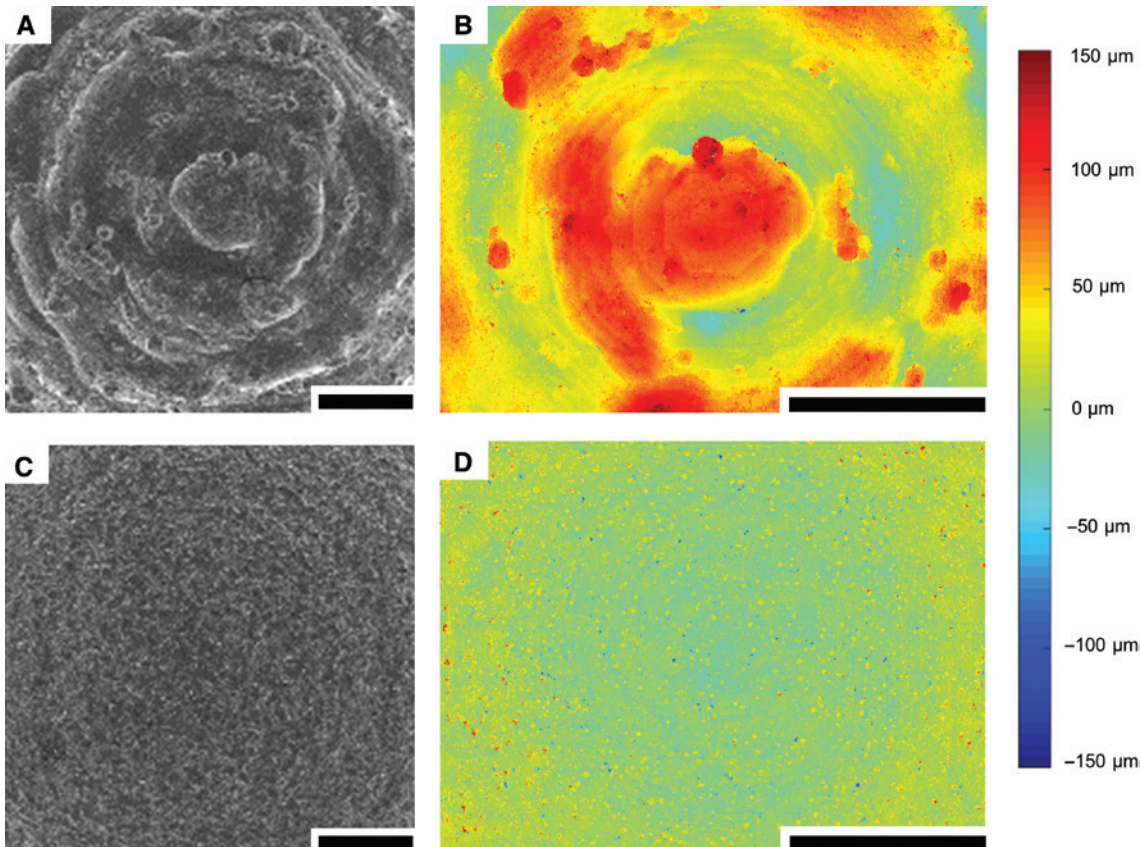


Figure 9: Half-sphere-shaped geometry: (A) SEM image (oblique view) of the raw LPBF-generated part. (B) Deviation of the raw part from the target geometry measured by LSM. (C) SEM image (oblique view) of post-processed part. (D) Deviation of the post-processed part from target geometry measured by LSM. Scale bars represent a length of 500 μm . Laser wavelength $\lambda_{\text{pl}} = 1030 \text{ nm}$, pulse duration $\tau_{\text{p}} = 600 \text{ fs}$, peak fluence $\Phi_0 = 3.5 \text{ J/cm}^2$, repetition rate $f_{\text{p}} = 70 \text{ kHz}$, feed rate $v = 560 \text{ mm/s}$.

4 Conclusion

In summary, we presented a post-processing method for LPBF-generated aluminum parts based on OCT closed-loop controlled laser ablation with ultrashort laser pulses that can be used to reduce the surface roughness and the shape deviations. The surface roughness was reduced by about 67% to $S_a = 4.6 \pm 0.3 \mu\text{m}$ by applying a suitable peak fluence in the range of 1.7 J/cm^2 – 2.6 J/cm^2 in order to avoid cavities or protrusions on the surface while minimizing surface defects. The OCT-based measurements were used for both precise positioning of the raw part and determination of the areas where further ablation is required to reach the targeted net shape. Post-processing by closed-loop controlled ablation reduced the mean deviation of the manufactured part from the target geometry by 63%–77% for different shapes such as cone, pyramid, steps, and a half sphere. Precise manufacturing of geometrical features like thin tips, smooth inclined surfaces, and pronounced edges was realized using the presented post-processing

method. Future work will include the removal of support structures and integration of functional structures by laser ablation into the manufactured parts.

Acknowledgment: The authors thank Markus Kogel-Holacher and Precitec for the loan of the OCT-based measurement system CHRcodile 2, Fibercryst for the loan of the ultrafast laser Femto 30, and Trumpf for the deployment of the LPBF machine TruPrint 3000 as part of the project GrantSLAM and in cooperation with GSaME. Furthermore, the authors thank Johannes Wahl for the SEM images and Gennadij Nikitin for the LSM measurements.

References

- [1] F. Froes, R. Boyer, and B. Dutta, in ‘Additive Manufacturing for the Aerospace Industry’ (Elsevier, Amsterdam, Netherlands, 2019) pp. 1–6.
- [2] C. Emmelmann, M. Petersen, J. Kranz and E. Wycisk, Proc. SPIE 8065, 1–12 (2011).

- [3] H. Hassanin, A. Elshaer, R. Benhadj-Djilali, F. Modica and I. Fassi, in 'Micro and Precision Manufacturing' (Springer, Cham, Switzerland, 2018) pp. 145–164.
- [4] Z. Zhu, S. Keimasi, N. Anwer, L. Mathieu and L. Qiao, in 'Advances on Mechanics, Design Engineering and Manufacturing' (Springer, Cham, Switzerland, Springer, 2017) pp. 241–250.
- [5] N. Kumbhar and A. Mulay, *J. Inst. Eng. (India): Series C* 99, 481–487 (2018).
- [6] J. Schanz, M. Hofele, L. Hitzler, M. Merkel and H. Riegel, in 'Machining, Joining and Modifications of Advanced Materials' (Springer, Singapore, 2016) pp. 159–169.
- [7] M. Hofele, J. Schanz, B. Burzic, S. Lutz, M. Merkel, et al., in 'Lasers in Manufacturing Conference' pp. 1–12, 2017.
- [8] S. Campanelli, G. Casalino, N. Contuzzi and A. Ludovico, *Procedia CIRP* 12, 462–467 (2013).
- [9] I. Mingareev, T. Bonhoff, A. F. El-Sherif, W. Meiners, I. Kelbassa, et al., *J. Laser Appl.* 25, 052009-1–052009-4 (2013).
- [10] D. Holder, S. Boley, M. Buser, C. Irion, R. Weber, et al., in 'Lasers in Manufacturing Conference,' pp. 1–6, 2019.
- [11] P. Webster, L. Wright, Y. Ji, C. Galbraith, A. Kinross, et al., *Opt. Lett.* 39, 6217–6220 (2014).
- [12] S. Boley, D. Holder, V. Onuseit, T. Graf, M. Buser, et al., in 'Lasers in Manufacturing Conference', pp. 1–9, 2017.
- [13] D. Holder, S. Boley, M. Buser, R. Weber and T. Graf, in '10th CIRP Conference on Photonic Technologies LANE 2018', 74, 557–561 (2018).
- [14] R. Schares, S. Schmitt, M. Emonts, K. Fischer, R. Moser, et al., in 'Proceedings of SPIE, High Power Laser Materials Processing: Applications, Diagnostics, and Systems', 7, 1–12 (2018).
- [15] S. Faas, U. Bielke, R. Weber and T. Graf, *Appl. Phys. A* 124, 1–9, (2018).
- [16] D. Büche, S. Klostermann, G. Rogé and X. Loyatho, in 'Uncertainty Management for Robust Industrial Design in Aeronautics' (Springer Nature, Cham, Switzerland, 2019) pp. 35–51.
- [17] J. Fishburn, M. Withford, D. Coutts and J. Piper, *Appl. Surf. Sci.* 252, 5182–5188 (2006).
- [18] K. Kurselis, R. Kiyam and B. N. Chichkov, *Appl. Surf. Sci.* 258, 8845–8852 (2012).
- [19] A. Salama, Y. Yan, L. Li, P. Mativenga, D. Whitehead, et al., *Mater. Des.* 107, 461–469 (2016).
- [20] C. He, F. Zibner, C. Fornaroli, J. Ryll, J. Holtkamp, et al., *Phys. Procedia* 56, 1066–1072 (2014).
- [21] T. Graf, M. Abdou Ahmed, P. Berger, V. Onuseit and R. Weber, *Industrial Laser Solutions* 13–15, (2019). <https://www.industrial-lasers.com/cutting/article/16484556/the-laser-one-universal-tool-for-manufacturing>.